Physics-Infused Reduced-Order Modeling for Analysis of Ablating Hypersonic Thermal Protection Systems

November 15, 2025

Abstract

This work presents a *physics-infused reduced-order modeling* (PIROM) framework towards the design, analysis, and optimization of non-decomposing ablating hypersonic thermal protection systems (TPS). It is demonstrated via the modeling of transient thermo-ablative behavior of non-decomposing multi-layered hypersonic TPS. The PIROM architecture integrates a reduced-physics backbone, based on the lumped-capacitance model (LCM), with data-driven correction dynamics formulated via a coarse-graining approach rooted in the Mori-Zwanzig formlism. The LCM is coupled to a surface velocity model (SVM) to capture the recession of the ablating TPS as a function of the surface temperature. While the LCM and SVM capture the dominant physics of the ablating TPS response, the correction terms compensate for residual dynamics arising from higher-order non-linear interactions and heterogeneities across material layers. The PIROM consistently achieves errors below 1% for a wide range of extrapolative settings of design parameters involving time-and-space varying boundary conditions and SVM models, and improves by x % over the LCM alone. Moreover, the PIROM delivers online evaluations that are two orders of magnitude faster than the full-order model (FOM). These results demonstrate that PIRO effectively reconciles the trade-offs between accuracy, generalizability, and efficiency, providing a promising framework for optimizing multi-physical dynamical systems, such as TPS under diverse operating conditions.

1 Introduction

At hypersonic speeds, aerospace vehicles experience extreme aero-thermo-dynamic environments that require specialized thermal protection systems (TPS) to shield internal substructures, electronics, and possibly crew members from the intense aerodynamic heating.

The TPS is often composed of ablating materials – a high-temperature capable fibrous material injected with a resin that fills the pore network and strengthens the composite Amar2016. The TPS design promotes the exchange of mass through thermal and chemical reactions (i.e., pyrolisis), effectively mitigating heat transfer to the sub-structures.

As a result, accurate prediction for the ablating TPS response under extreme hypersonic heating becomes fundamental to ensuring survivability, performance, and safety of hypersonic vehicles. Not only is it necessary to assess the performance of the thermal management systems, but also the shape changes of the vehicle's outer surface induced by the ablating material, and its impact on the aerodynamics, structural integrity, and controllability. Nonetheless, high-fidelity simulations of ablating TPS remains a formidable challenge both theoretically and computationally.

Unfortunately, high-fidelity simulations of ablating TPS remains a formidable challenge both theoretically and computationally.

On the theoretical side, the thermo-chemical reactions, coupled with the irregular pore network structure, translate into simplifying assumptions to reduce non-linearities, and make the resulting equations more amenable for engineering application and design analysis x. For instance, one of the most notable codes is the one-dimensional CMA code that was developed by Aerotherm Corporation in the 1960s Howard2015. Despite its practical use in...

Another example is the CHarring Ablator Response (CHAR) ablation code, which ignores elemental decompositions of the pyrolizing gases, assumes the gases to be a mixture of perfect gases in thermal equilibrium, and assumes no reaction or condensation with the porous network [1].

theoretically:

computationally:

2 Modeling of Ablating Thermal Protection Systems

This section presents the problem of modeling a non-decomposing ablating TPS subjected to extreme hypersonic heating. Two different but mathematically connected solution strategies are provided: (1) a high-fidelity full-order model (FOM) based on a finite element method (FEM), and (2) a low-fidelity reduced-physics model (RPM) based on a lumped capacitance model (LCM) and a one-dimensional surface velocity model (SVM). The FOM is computationally expensive but provides the highest fidelity, while the RPM is computationally efficeint but has low predictive fidelity; both models are amenable to high-dimensional design variables. The RPM is used in the subsequent sections for deriving the PIROM.

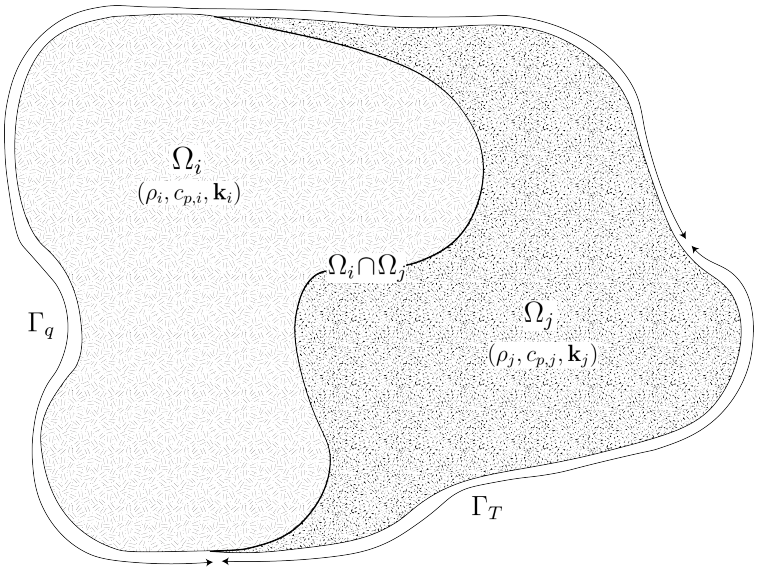

Figure 1: General domain Ω with prescribed Neumann and Dirichlet boundary conditions on Γ_q and Γ_T. Mesh displacement $w(x,t)$ occurs on the Γ_q boundary.

2.1 Governing Equations

The multi-physics for a non-decomposing ablating TPS involves the *energy equation* which models the transient heat conduction inside the TPS, and the *pseudo-elasticity equation*, which models the mesh motion due to surface recession. The governing PDEs for the ablating TPS are summarized in this section.

2.1.1 Energy Equation

Consider a generic domain $\Omega \subset$, $d = 2$ or 3, illustrated in Fig. 1. Let $\partial\Omega = \Gamma_q \cup \Gamma_T$ and $\Gamma_q \cap \Gamma_T = \emptyset$, where a Neumann $q_b(x,t)$ boundary condition is prescribed on the Γ_q boundary, and represents the surface exposed to the hypersonic boundary layer. The Dirichlet $T_b(x,t)$ boundary condition is prescribed on the boundary Γ_T. The TPS is divided into N non-overlapping components $\{\Omega_i\}_{i=1}^N$, as illustrated in Fig. 1 for $N = 2$. The i-th component Ω_i is associated with material properties $(\rho_i, c_{p,i}, \mathbf{k}_i)$, that are assumed to be continuous within one component, and can be discontinuous across two neighboring components.

The transient heat conduction is described by the energy equation,

$$\rho c_p \left(\frac{\partial T}{\partial t} + \tilde{\mathbf{v}}(x,t) \cdot \nabla T \right) - \nabla \cdot (\mathbf{k} \nabla T) = 0, \ x \in \Omega \tag{1a}$$

$$-\mathbf{k} \nabla T \cdot \mathbf{n} = q_b(x,t), \ x \in \Gamma_q \tag{1b}$$

$$T(x,t) = T_b(x,t), \ x \in \Gamma_T \tag{1c}$$

$$T(x,0) = T_0(x), \ x \in \Omega \tag{1d}$$

where the density ρ is constant, while the heat capacity c_p and thermal conductivity $\mathbf{k} \in \mathbb{R}^{d \times d}$ may depend on temperature. In the order they appear, the terms in eq. (1a) include, the unsteady energy storage, heat conduction, temperature advection due to mesh motion, and source terms due to boundary conditions. The boundary conditions for the energy equation includes Neumann eq. (1b) and Dirichlet eq. (1c) on Γ_T.

An Abirtrary Lagrangian-Eulerian (ALE) description is used to account for mesh motion due to surface recession, where $\tilde{\mathbf{v}}(x,t)$ is the relative velocity of the material with respect to the mesh,

$$\tilde{\mathbf{v}}(x,t) = \mathbf{v}_s(x,t) - \mathbf{v}_m(x,t) \tag{2}$$

where $\mathbf{v}_s(x,t)$ and $\mathbf{v}_m(x,t)$ are the physical material velocity and mesh velocity, respectively. In this work, the physical material velocity is assumed to be zero, i.e., $\mathbf{v}_s(x,t) = \mathbf{0}$, and thus the relative velocity is simply the negative of the mesh velocity, $\tilde{\mathbf{v}}(x,t) = -\mathbf{v}_m(x,t)$.

2.1.2 Pseudo-Elasticity Equation

The mesh motion is described by the steady-state pseudo-elasticity equation without body forces,

$$\nabla \cdot \boldsymbol{\sigma}(\mathbf{w}) = \mathbf{0}, \quad \forall\, t \in \mathcal{T},\ \mathbf{x} \in \Omega \tag{3a}$$

$$\mathbf{w}(\mathbf{x},t) = \mathbf{w}_q(\mathbf{x},t), \quad \forall\, t \in \mathcal{T},\ \mathbf{x} \in \Gamma_q \tag{3b}$$

$$\mathbf{w}(\mathbf{x},t) = \mathbf{0}, \quad \forall\, t \in \mathcal{T},\ \mathbf{x} \notin \Gamma_q \tag{3c}$$

$$\mathbf{w}(\mathbf{x},0) = \mathbf{0}, \quad \forall\, \mathbf{x} \in \Omega \tag{3d}$$

where the stress tensor $\boldsymbol{\sigma}$ is related to the strain tensor $\boldsymbol{\epsilon}(\mathbf{w})$ through Hooke's law,

$$\boldsymbol{\sigma}(\mathbf{w}) = \mathbb{D} : \boldsymbol{\epsilon}(\mathbf{w})$$

where $\mathbb{D}$ is the fourth-order positive definite elasticity tensor, and ":" is the double contraction of the full-order tensor $\mathbb{D}$ with the second-order tensor $\boldsymbol{\epsilon}$. The elasticity tensor

ordinarily possess a number of symmetries, effectively reducing the number of components that describe it [2]. The symmetric strain tensor $\boldsymbol{\epsilon}$ measures the deformation of the mesh due to displacements $\mathbf{w}(x,t)$, and is defined as,

$$\boldsymbol{\epsilon}(\mathbf{w}) = \frac{1}{2}\left(\nabla\mathbf{w} + \nabla\mathbf{w}^\top\right)$$

The "material" properties for the mesh are chosen to tailor the mesh deformation, and need not represent the actual material being modeled [1].

For the pseudo-elasticity equations, the boundary conditions include prescribed displacements $\mathbf{w}_q(x,t)$ on the heated boundary Γ_q in eq. (3b), and zero displacements on the unheated boundaries in eq. (3c). The initial condition for the mesh displacements is zero in eq. (3d). Particularly, the surface velocity due to the ablating material is a function of the surface temperature $T_q(x,t)$ for $x \in \Gamma_q$ on the heated boundary. For the i-th material component, the mesh velocity on the heated boundary is imposed based on the following relation,

$$\hat{\mathbf{n}} \cdot \mathbf{v}_m(x,t) = f(T_q(x,t)), \quad x \in \Gamma_q \tag{4}$$

where $\hat{\mathbf{n}}$ is the unit normal vector on the heated boundary Γ_q, and f is a function obtained from tabulated data for the material, commonly referred to as a B' table [1]. The B' table provides a model for the recession velocity as a function of the surface temperature, and is pre-computed based on high-fidelity simulations of the ablation process for a one-dimensional slab of the material, and is independent of the TPS geometry. Provided the surface velocity, the boundary condition in eq. (5) for the mesh displacements are computed by integrating the surface velocity over time,

$$\mathbf{w}_q(x,t) = \int_0^t \mathbf{v}_m(x,\tau)d\tau \tag{5}$$

2.2 Full-Order Model: Finite-Element Method

To obtain the full-order numerical solution, the *energy equation* is spatially discretized using variational principles of the Discontinuous Galerkin (DG) method [3]. Note that the choice of DG approach is mainly for theoretical convenience, and is exclusively performed on the energy equation, as it is the surface temperature that drives the ablation process. The equivalence between DG and FEM is noted upon their convergence. For the *pseudo-elasticity equation* standard FEM is used to compute the mesh displacements based on the surface temperature provided by the DG solution of the energy equation [2].

Consider a conforming mesh partition domain, where each element belongs to one and

only one component. Denote the collection of all M elements as $\{E_i\}_{i=1}^{M}$. In an element E_i, its shared boundaries with another element E_j, Neumann BC, and Dirichlet BC are denoted as e_{ij}, e_{iq}, and e_{iT}, respectively. Lastly, $|e|$ denotes the length ($n_d = 2$) or area ($n_d = 3$) of a component boundary e.

For the i-th element, use a set of P trial functions, such as polynomials, to represent the temperature distribution,

$$T_i(x,t) = \sum_{l=1}^{P} \phi_l^i(x) u_l^i(t) \equiv \boldsymbol{\phi}_i^\top(x)\mathbf{u}_i(t), \quad i = 1, 2, \ldots, M \tag{6}$$

Without loss of generality, the trial functions are assumed to be orthogonal, so that,

$$\int_{E_i} \phi_l^i(x)\phi_k^i(x)d\Omega = 0, \quad l \neq k$$

where δ_{lk} is the Kronecker delta function. Furthermore, for simplicity, choose $\phi_1^i = 1$. Thus, by orthogonality,

$$\int_{E_i} \phi_1^i(x)d\Omega = |E_i|, \quad \int_{E_i} \phi_k^i(x)d\Omega = 0, \quad k = 2, 3, \ldots, P$$

Under the choice of basis functions, u_1^i is simply the average temperature of element E_i, denoted as $\bar{u}_i$.

By standard variational processes, e.g., [3], the element-wise governing equation is denoted as,

$$\mathbf{A}_i\dot{\mathbf{u}}_i = (\mathbf{B}_i + \mathbf{C}_i)\,\mathbf{u}_i + \sum_{j\in\mathcal{N}_i\cup\{T_b\}} \left(\mathbf{B}_{ij}^i\mathbf{u}_i + \mathbf{B}_{ij}^j\mathbf{u}_j\right) + \mathbf{f}_i(t), \quad \text{for } i = 1, 2, \ldots, M \tag{7}$$

which is collected as the following ODE for the all the elements in the mesh,

$$\mathbf{A}(\mathbf{u})\dot{\mathbf{u}} = [\mathbf{B}(\mathbf{u}) + \mathbf{C}(\mathbf{u})]\,\mathbf{u} + \mathbf{f}(t) \tag{8}$$

where $\mathbf{u} = [\mathbf{u}_1, \mathbf{u}_2, \ldots, \mathbf{u}_M]^\top \in \mathbb{R}^{MP}$ includes all the DG variables, $\mathbf{f} \in \mathbb{R}^{MP}$ is the external forcing, and the system matrices $\mathbf{A}$, $\mathbf{B}$, and $\mathbf{C}$ are the matrices due to heat capacity, heat conduction, and temperature advection due to mesh motion, respectively. A detailed derivation of eqs. (7) and (8) and their matrices is provided in Appendix A.

2.3 Reduced-Physics Model

The RPM for predicting the response of the ablating TPS consists of two components: (1) the *lumped-capacitance model* (LCM), and (2) the *surface velocity model* (SVM). The LCM is described as a first-order system of ODEs for predicting the average temperatures inside the components of the TPS, and provides a low-fidelity (under estimate) for the component's surface temperature. The SVM provides a relation between the surface temperature and the surface recession velocity based on pre-computed B' tables for the material, enabling the computation of one-dimensional surface displacements. The LCM and SVM are combined to define the RPM, providing low-fidelity estimates for the temperatures and surface recession of the ablating TPS.

2.3.1 Lumped Capacitance Model

A general form of the LCM is provided in this section; details regarding the derivation for the four-component TPS in Fig. 2 are provided in Appendix A. The LCM is a classical physics-based low-order model for predicting the temporal variation of average temperature in multiple interconnected components [4]. The LCM is derived at the component level from a point of view of energy conservation, and leads to the following system of ODEs for the average temperatures on the components,

$$\bar{\mathbf{A}}\dot{\bar{\mathbf{u}}} = \bar{\mathbf{B}}\bar{\mathbf{u}} + \bar{\mathbf{f}}(t) \tag{9}$$

Where the states and inputs,

$$\bar{\mathbf{u}} = [\bar{u}_1, \bar{u}_2, \ldots, \bar{u}_N]^\top \in \mathbb{R}^N, \quad \bar{\mathbf{f}} = \left[\bar{f}_1, \bar{f}_2, \ldots, \bar{f}_N\right]^\top \in \mathbb{R}^N \tag{10}$$

include the average temperatures $\bar{\mathbf{u}}$ and spatially-integrated inputs $\bar{\mathbf{f}}$ for the N components. For $i, j = 1, 2, \ldots, N$ the (i,j)-th elements of the $\bar{\mathbf{A}} \in \mathbb{R}^{N\times N}$, $\bar{\mathbf{B}} \in \mathbb{R}^{N\times N}$, and $\bar{\mathbf{f}} \in \mathbb{R}^N$ matrices are given by,

$$\bar{A}_i = \begin{cases} \int_{\Omega_i} \rho c_p d\Omega_i, & i = j \\ 0, & i \neq j \end{cases}, \quad \bar{B}_{ij} = \begin{cases} \sum_{j\in\mathcal{N}_i\cup\{T_b\}} \bar{B}^i_{ij}, & i = j \\ \bar{B}^{(j)}_{ij}, & i \neq j \end{cases}, \tag{11a}$$

$$\mathbf{f}_i = \begin{cases} |e_{iq}|\bar{q}_i + \frac{|e_{iT}|}{R_i}\bar{T}_i, & i = j \\ 0, & i \neq j \end{cases} \tag{11b}$$

where,

$$\bar{q}_i = \frac{1}{|e_{iq}|}\int_{e_{iq}} q_b de_{iq}, \quad \bar{T}_i = \frac{1}{|e_{iT}|}\int_{e_{iT}} T_b de_{iT}, \quad \bar{B}^i_{ij} = -\frac{|e_{ij}|}{R_{ij}}, \quad \bar{B}^j_{ij} = \frac{|e_{ij}|}{R_{ij}} \tag{12}$$

where R_{ij} is the equivalent thermal resistance between two neighboring components Ω_i and Ω_j, and R_i is the thermal resistance between component Ω_i and the Dirichlet boundary. The thermal resistances are computed based on the geometry and material properties of the components; details regarding their computation are provided in Appendix A.

2.3.2 Surface Velocity Model

The displacement is assumed to be *one-dimensional* on the heated boundary Γ_q, i.e., the surface recedes only in the direction of the applied load. For example, in Fig. 2, the surface displacement on the heated boundary occurs only in the negative y-direction for the three components exposed to the hypersonic boundary layer; the fourth component is the substrate and does not ablate. Displacements along the x direction is small relative to displacements in the y direction, and are thus neglected.

For the i-th component, the SVM considered in this work takes the form,

$$\dot{\mathbf{w}} = \boldsymbol{\Xi}\bar{\mathbf{u}} - \tilde{\mathbf{f}} \tag{13}$$

where $\boldsymbol{\Xi} = \mathrm{diag}\,(\xi_1, \ldots, \xi_N)$ and $\tilde{\mathbf{f}} = (\xi_1\bar{u}_{0,1}, \ldots, \xi_N\bar{u}_{0,N})^\top$. The constants ξ_i are small material-dependent constants, determined from the B' table, and $\bar{u}_{0,i}$ is the constant initial temperature of the component. The SVM provides a relation between the surface temperature and the surface recession velocity based on pre-computed B' tables for the material.

2.3.3 Coupled Reduced-Physics Model

The LCM and SVM are combined to define the RPM for predicting the thermo-ablative response of the TPS under hypersonic boundary layers. Specifically, the RPM is defined as the LCM as in eq. (9), where the *geometry- and temperature-dependent matrices* $\bar{\mathbf{A}}$, $\bar{\mathbf{B}}$, and $\bar{\mathbf{f}}$ are updated at each time step based on the current temperature $\bar{\mathbf{u}}$ and displacements $\mathbf{w}$ provided by the SVM. The RPM is formally stated as,

$$\tilde{\mathbf{A}}(\mathbf{s})\dot{\mathbf{s}} = \tilde{\mathbf{B}}(\mathbf{s})\mathbf{s} + \tilde{\mathbf{F}}(t) \tag{14}$$

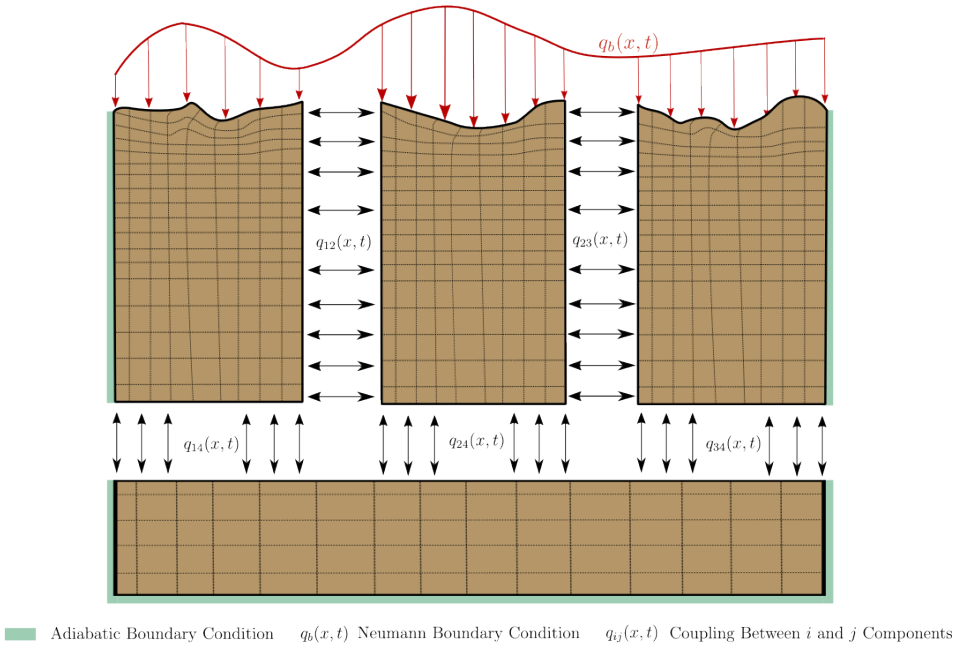

(a) TPS Decomposition

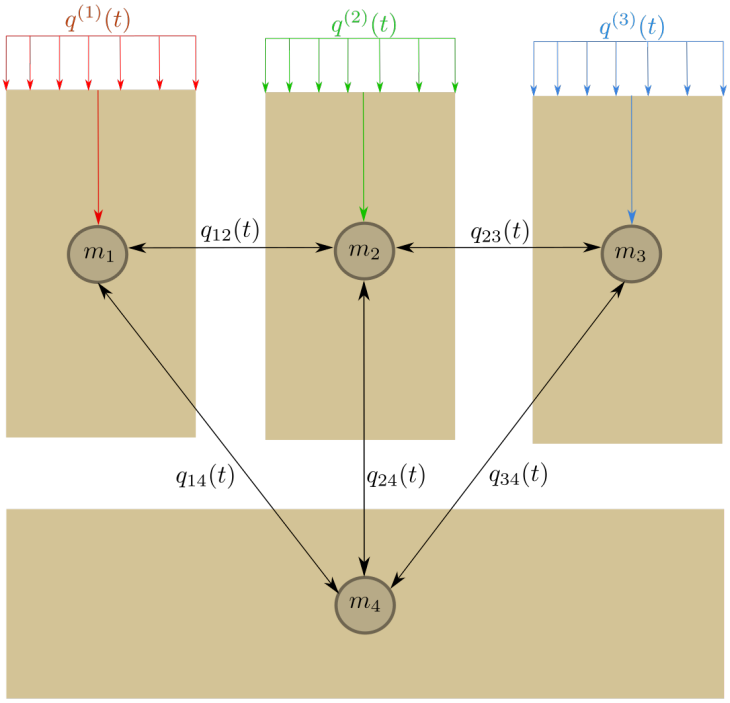

(b) Lumped Mass Representation

Figure 2: Partition of the TPS into three ablating and one non-ablating components with the corresponding lumped-mass representation.

where the state $\mathbf{s} = [\bar{\mathbf{u}}, \mathbf{w}]^\top \in \mathbb{R}^{2N}$ includes the average temperatures and one-dimensional surface displacements. The matrices are given as,

$$\tilde{\mathbf{A}}(\mathbf{s}) = \begin{bmatrix} \bar{\mathbf{A}}(\mathbf{s}) & \mathbf{0} \\ \mathbf{0} & \mathbf{I} \end{bmatrix}, \quad \tilde{\mathbf{B}}(\mathbf{s}) = \begin{bmatrix} \bar{\mathbf{B}}(\mathbf{s}) & \mathbf{0} \\ \boldsymbol{\Xi} & \mathbf{0} \end{bmatrix}, \quad \tilde{\mathbf{F}}(t) = \begin{bmatrix} \bar{\mathbf{f}}(t) \\ -\tilde{\mathbf{f}} \end{bmatrix} \tag{15}$$

In the matrices $\tilde{\mathbf{A}}$ and $\tilde{\mathbf{B}}$, the surface displacements $\mathbf{w}$ are used to define the dimensions for the Ω_i component used in eqs. (11b) and (12), thus effectively coupling the LCM and SVM.

2.4 Summary of Modeling Approaches

The FOM (i.e., DG-FEM) and RPM (i.e., LCM with SVM) are two different but mathematically connected solution strategies. Specifically, the LCM in eq. (9) not only resembles the functional form of the DG model in eq. (8), but can be viewed as a special case of the latter, where the mesh partition is extremely coarse, and the trial and test functions are piece-wise constants. This removes all spatial variations within each component, and neglects advection effects due to mesh motion.

For example, consider the case where each component Ω_i is treated as one single element, and each element employs one constant basis function $\phi_i = 1$. The element-wise DG model in eq. (7) simplifies into a scalar ODE,

$$\mathbf{A}^{(i)} = \bar{A}_i, \quad \mathbf{C}^{(i)} = 0, \quad \mathbf{B}_{ij}^{(i)} = -\sigma|e_{ij}|, \quad \mathbf{B}_{ij}^{(j)} = \sigma|e_{ij}|, \quad \mathbf{f}_i = |e_{iq}|\bar{q}_i + \sigma|e_{iT}|\bar{T}_i \tag{16}$$

Clearly, the LCM is a coarse zeroth-order DG model with the inverse of thermal resistance chosen as the element-wise penalty factors. Or conversely, the DG model is a refined version of LCM via *hp*-adaptation.

The FOM and RPM represent two extremes in the modeling fidelity and computational cost spectrum. On one hand, the FOM is the most accurate but computationally expensive to evaluate due to the fine mesh discretizations for both the temperature and displacement fields, leading to possibly millions of state variables. On the other hand, the RPM considers only the average temperature of the material from which one-dimensional surface displacements are computed. This considerably reduces the computational cost, but sacrifices local temperature information that are critical to properly capture higher-order effects due to mesh motion and thermal gradients within each component. Thus, neither the FOM nor the RPM is an universal approach for real-world analysis, design, and optimization tasks for ablating TPS, where thousands of high-fidelity model evaluations may be necessary. This issue motivates the development of the PIROM, which can achieve the fidelity of FOM at

a computational cost close to the RPM, while maintaining the generalizability to model parameters.

3 Physics-Infused Reduced-Order Modeling

The formulation of PIROM for ablating TPS starts by connecting the FOM, i.e., the DG-FEM, and the RPM, i.e., the LCM, via a coarse-graining procedure. This procedure pinpoints the missing dynamics in the LCM when compared to DG-FEM. Subsequently, the Mori-Zwanzig (MZ) formalism is employed to determine the model form for the missing dynamics in PIROM. Lastly, the data-driven identification of the missing dynamics in PIROM is presented.

3.1 Deriving the Reduced-Physics Model via Coarse-Graining

The subsequent coarse-graining formulation is performed on the DG-FEM in eq. (8) to derive the LCM in eq. (9). This process constraints the trial function space of a full-order DG model to a subset of piece-wise constants, so that the variables $\mathbf{u}$, matrices $\mathbf{A}$, $\mathbf{B}$, and $\mathbf{C}$, and forcing vector $\mathbf{f}$ are all approximated using a single state associated to the average temperature. Note that the coarse-graining is exclusively performed on the thermal dynamics, as it is the surface temperature that drives the one-dimensional recession via the SVM. Hence, the coarse-graining of the mesh dynamics is not included in the following procedure.

3.1.1 Coarse-Graining of States

Consider a DG model as in eq. (8) for M elements and an LCM as in eq. (9) for N components; clearly $M \gg N$. Let $\mathcal{V}_j = \left\{ i \middle| E_i \in \Omega_j \right\}$ be the indices of the elements belonging to the j-th component, so $E_i \in \Omega_j$ for all $i \in \mathcal{V}_j$. The number of elements in the j-th component is $|\mathcal{V}_j|$. The average temperature on Ω_j is,

$$\bar{u}_j = \frac{1}{|\Omega_j|} \sum_{i \in \mathcal{V}_j} \int_{E^{(i)}} \boldsymbol{\phi}^{(i)}(x)^T \mathbf{u}^{(i)} d\Omega = \frac{1}{|\Omega_j|} \sum_{i \in \mathcal{V}_j} |E_i| \, \boldsymbol{\varphi}_i^{j\top} \mathbf{u}^{(i)}, \quad j = 1, 2, \ldots, N \tag{17}$$

where $|\Omega_j|$ and $|E_i|$ denote the area ($d = 2$) or volume ($d = 3$) of component j and element i, respectively. The orthogonal basis functions are defined as $\boldsymbol{\varphi}_i^{j\top} = [1, 0, \ldots, 0]^\top \in \mathbb{R}^P$.

Conversely, given the average temperatures of the N components, $\bar{\mathbf{u}}$, the states of an

arbitrary element E_i is written as,

$$\mathbf{u}^{(i)} = \sum_{k=1}^{N} \boldsymbol{\varphi}_i^k \bar{u}_k + \delta\mathbf{u}^{(i)}, \quad i = 1, 2, \ldots, M \tag{18}$$

where $\boldsymbol{\varphi}_i^k = 0$ if $i \notin \mathcal{V}_k$, and $\delta\mathbf{u}^{(i)}$ represents the deviation from the average temperature and satisfies the orthogonality condition $\boldsymbol{\varphi}_i^{k\top}\delta\mathbf{u}^{(i)} = 0$ for all k.

Equations eqs. (17) and (18) are combined and written in matrix form as,

$$\bar{\mathbf{u}} = \boldsymbol{\Phi}^{+}\mathbf{u}, \quad \mathbf{u} = \boldsymbol{\Phi}\mathbf{u} + \delta\mathbf{u} \tag{19}$$

where $\boldsymbol{\Phi} \in \mathbb{R}^{MP\times N}$ is a matrix of $M \times N$ blocks, with the (i, j)-th block as $\boldsymbol{\varphi}_i^j$, $\boldsymbol{\Phi}^{+} \in \mathbb{R}^{N\times MP}$ is the left inverse of $\boldsymbol{\Phi}$, with the (i, j)-th block as $\boldsymbol{\varphi}_i^{j+} = \frac{|E_i|}{|\Omega_j|}\boldsymbol{\varphi}_i^{j\top}$, and $\delta\mathbf{u}$ is the collection of deviations. By their definitions, $\boldsymbol{\Phi}^{+}\boldsymbol{\Phi} = \mathbf{I}$ and $\boldsymbol{\Phi}^{+}\delta\mathbf{u} = \mathbf{0}$.

3.1.2 Coarse-Graining of Dynamics

In this section, the dependence of the matrices with respect to the displacements $\mathbf{w}$ is dropped to isolate the analysis based on coarsened variables. Next, consider a function of states in the form of $\mathbf{M}(\mathbf{u})\,\mathbf{g}(\mathbf{u})$, where $\mathbf{g} : \mathbb{R}^{MP} \to \mathbb{R}^{MP}$ is a vector-valued function, and $\mathbf{M} : \mathbb{R}^{MP} \to \mathbb{R}^{p\times MP}$ is a matrix-valued function with an arbitrary dimension p. Define the projection matrix $\mathbf{P} = \boldsymbol{\Phi}\boldsymbol{\Phi}^{+}$ and the projection operator $\mathcal{P}$ as,

$$\begin{aligned}\mathcal{P}\left[\mathbf{M}(\mathbf{u})\mathbf{g}(\mathbf{u})\right] &= \mathbf{M}\left(\mathbf{P}\mathbf{u}\right)\mathbf{g}\left(\mathbf{P}\mathbf{u}\right)\\ &= \mathbf{M}\left(\boldsymbol{\Phi}\bar{\mathbf{u}}\right)\mathbf{g}\left(\boldsymbol{\Phi}\bar{\mathbf{u}}\right)\end{aligned} \tag{20}$$

so that the resulting function depends only on the average temperatures $\bar{\mathbf{u}}$. Correspondingly, the residual operator $\mathcal{Q} = \mathcal{I} - \mathcal{P}$, and $\mathcal{Q}\left[\mathbf{M}(\mathbf{u})\mathbf{g}(\mathbf{u})\right] = \mathbf{M}(\mathbf{u})\mathbf{g}(\mathbf{u}) - \mathbf{M}\left(\boldsymbol{\Phi}\bar{\mathbf{u}}\right)\mathbf{g}\left(\boldsymbol{\Phi}\bar{\mathbf{u}}\right)$. When the function is not separable, the projection operator is simply defined as $\mathcal{P}\left[\mathbf{g}(\mathbf{u})\right] = \mathbf{g}\left(\mathbf{P}\mathbf{u}\right)$.

Subsequently, the operators defined above are applied to coarse-grain the dynamics. First, write the DG-FEM in eq. (8) as,

$$\dot{\mathbf{u}} = \mathbf{A}(\mathbf{u})^{-1}\mathbf{B}(\mathbf{u})\mathbf{u} + \mathbf{A}(\mathbf{u})^{-1}\mathbf{C}(\mathbf{u})\mathbf{u} + \mathbf{A}(\mathbf{u})^{-1}\mathbf{f}(t) \tag{21}$$

and multiply both sides by $\boldsymbol{\Phi}^{+}$ to obtain,

$$\boldsymbol{\Phi}^{+}\dot{\mathbf{u}} = \boldsymbol{\Phi}^{+}\left(\boldsymbol{\Phi}\dot{\bar{\mathbf{u}}} + \delta\dot{\mathbf{u}}\right) = \dot{\bar{\mathbf{u}}} = \boldsymbol{\Phi}^{+}\mathbf{r}(\mathbf{u}, t) \tag{22}$$

Apply the projection operator $\mathcal{P}$ and the residual operator $\mathcal{Q}$ to the right-hand side to obtain,

$$\dot{\bar{\mathbf{u}}} = \mathcal{P}\left[\mathbf{\Phi}^{+}\mathbf{r}(\mathbf{u},t)\right] + \mathcal{Q}\left[\mathbf{\Phi}^{+}\mathbf{r}(\mathbf{u},t)\right] \equiv \mathbf{r}^{(1)}(\mathbf{u},t) + \mathbf{r}^{(2)}(\mathbf{u},t) \tag{23}$$

where $\mathbf{r}^{(1)}(\mathbf{u},t)$ is resolved dynamics that depends on $\bar{\mathbf{u}}$ only, and $\mathbf{r}^{(2)}(\mathbf{u},t)$ is the un-resolved or residual dynamics. Detailed derivations and analysis of $\mathbf{r}^{(1)}(\mathbf{u},t)$ and $\mathbf{r}^{(2)}(\mathbf{u},t)$ can be found in the Appendix.

It follows from Ref. [8] that the resolved dynamics is exactly the LCM, where the advection term reduces to zero, i.e., $\bar{\mathbf{C}}(\bar{\mathbf{u}}) = \mathbf{0}$ as shown in the Appendix. Using the notation from eq. (9), it follows that,

$$\begin{aligned}\mathbf{r}^{(1)}(\mathbf{u},t) &= \bar{\mathbf{A}}(\bar{\mathbf{u}})^{-1}\bar{\mathbf{B}}(\bar{\mathbf{u}})\bar{\mathbf{u}} + \bar{\mathbf{A}}(\bar{\mathbf{u}})^{-1}\bar{\mathbf{C}}(\bar{\mathbf{u}})\bar{\mathbf{u}} + \bar{\mathbf{A}}(\bar{\mathbf{u}})^{-1}\bar{\mathbf{f}}(\bar{\mathbf{u}}) \\ &= \bar{\mathbf{A}}(\bar{\mathbf{u}})^{-1}\bar{\mathbf{B}}(\bar{\mathbf{u}})\bar{\mathbf{u}} + \bar{\mathbf{A}}(\bar{\mathbf{u}})^{-1}\bar{\mathbf{f}}(t)\end{aligned} \tag{24}$$

where the following relations hold,

$$\bar{\mathbf{A}}(\bar{\mathbf{u}}) = \mathbf{W}\left(\mathbf{\Phi}^{+}\mathbf{A}\left(\mathbf{\Phi}\bar{\mathbf{u}}\right)^{-1}\mathbf{\Phi}\right)^{-1} \qquad \bar{\mathbf{C}}(\bar{\mathbf{u}}) = \mathbf{0} \tag{25a}$$

$$\bar{\mathbf{B}}(\bar{\mathbf{u}}) = \mathbf{W}\mathbf{\Phi}^{+}\mathbf{B}\left(\mathbf{\Phi}\bar{\mathbf{u}}\right)\mathbf{\Phi} \qquad \bar{\mathbf{f}}(t) = \mathbf{W}\mathbf{\Phi}^{+}\mathbf{f} \tag{25b}$$

where $\mathbf{W} \in \mathbb{R}^{N\times N}$ is a diagonal matrix with the i-th element as $[\mathbf{W}]_{ii} = |\mathcal{V}_k|$ if $i \in \mathcal{V}_k$. The examination of the second residual term $\mathbf{r}^{(2)}(\mathbf{u},t)$ in eq. (23) is shown in the Appendix, and demonstrates that the physical sources of missing dynamics in the LCM include: the approximation of non-uniform temperature within each component as a constant, and the elimination of the advection term due to coarse-graining. In sum, the above results not only show that the LCM is a result of coarse-graining of the full-order DG-FEM, but also reveal the discrepancies between the LCM and the DG-FEM. These discrepancies propagate into the SVM, which as a result of the averaging in the LCM formulation, under-predicts the surface recession rates. In the subsequent section, the discrepancies in the LCM are corrected to formulate the PIROM.

3.2 Physics-Infusion Via Mori-Zwanzig Formalism

The Mori-Zwanzig (MZ) formalism is an operator-projection technique used to derive ROMs for high-dimensional dynamical systems, especially in statistical mechanics and fluid dynamics [5, 6, 7]. It provides an exact reformulation of a high-dimensional Markovian dynamical system, into a low-dimensional observable non-Markovian dynamical system. The proposed ROM is subsequently developed based on the approximation to the non-Markovian term in

the observable dynamics. Particularly, eq. (23) shows that the DG-FEM dynamics can be decomposed into the resolved dynamics $\mathbf{r}^{(1)}(\mathbf{u}, t)$ and the orthogonal dynamics $\mathbf{r}^{(2)}(\mathbf{u}, t)$, in the sense of $\mathcal{P}\mathbf{r}^{(2)} = 0$. In this case, the MZ formalism can be invoked to express the dynamics $\bar{\mathbf{u}}$ in terms of $\bar{\mathbf{u}}$ alone as the projected Generalized Langevin Equation (GLE) [5, 6, 7],

$$\dot{\bar{\mathbf{u}}}(t) = \mathbf{r}^{(1)}(\bar{\mathbf{u}}, t) + \int_0^t \tilde{\boldsymbol{\kappa}}(t, s, \bar{\mathbf{u}}) ds \tag{26}$$

where the first and second terms are referred to as the Markovian and non-Markovian terms, respectively. The non-Markovian term accounts for the effects of past un-resolved states on the current resolved states via a memory kernel $\tilde{\boldsymbol{\kappa}}(t, s, \bar{\mathbf{u}})$, which in practice is computationally expensive to evaluate.

3.2.1 Markovian Reformulation

This section details the formal derivation of the PIROM for the thermal dynamics, based on approximations to the memory kernel. Specifically, the kernel $\tilde{\boldsymbol{k}}$ is examined via a leading-order expansion, based on prior work [9]; this can be viewed as an analog of zeroth-order holding in linear system theory with a sufficiently small time step. In this case, the memory kernel is approximated as,

$$\tilde{\boldsymbol{\kappa}}(t, s, \bar{\mathbf{u}}) \approx \mathbf{r}^{(1)}(\bar{\mathbf{u}}, t) \cdot \nabla_{\bar{\mathbf{u}}} \mathbf{r}^{(2)} \left(\boldsymbol{\Phi}\bar{\mathbf{u}}, t\right) \tag{27}$$

Note that the terms in $\mathbf{r}^{(1)}$ have a common factor $\bar{\mathbf{A}}^{-1}$; this motivates the following heuristic modification of the model form in eq. (26),

$$\dot{\bar{\mathbf{u}}} = \mathbf{r}^{(1)}(\bar{\mathbf{u}}, t) + \bar{\mathbf{A}}^{-1}(\bar{\mathbf{u}}) \int_0^t \boldsymbol{\kappa}(t, s, \bar{\mathbf{u}}) ds \tag{28a}$$

$$\bar{\mathbf{A}}(\bar{\mathbf{u}})\dot{\bar{\mathbf{u}}} = \bar{\mathbf{B}}\left(\bar{\mathbf{u}}\right)\bar{\mathbf{u}} + \bar{\mathbf{f}}(t) + \int_0^t \boldsymbol{\kappa}(t, s, \bar{\mathbf{u}}) ds \tag{28b}$$

where the original kernel $\tilde{\boldsymbol{\kappa}}$ is effectively normalized by $\bar{\mathbf{A}}^{-1}$. Intuitively, such choice of kernel reduces its dependency on the averaged material properties, and simplifies the subsequent design of model form.

Subsequently, the hidden states are introduced to "Markovianize" the system eq. (26). In this manner, eq. (28b) is converted into a pure state-space model, with the functional form of the LCM retained; since LCM is a physics-based model, then it encodes the physical information and retains explicit parametric dependence of the problem. Consider the

representation of the kernel as a finite sum of simpler functions, e.g., exponentials,

$$\boldsymbol{\kappa}(t,s,\bar{\mathbf{u}}) = \sum_{j=1}^{m} \mathcal{K}_j(t,s,\bar{\mathbf{u}}) \left[\mathbf{p}_j + \mathbf{d}_j(\bar{\mathbf{u}})\right] \phi_j(s,\bar{\mathbf{u}}) \tag{29}$$

where,

$$\mathcal{K}_j(t,s,\bar{\mathbf{u}}) = e^{-\int_s^t (\lambda_j + e_j(\bar{\mathbf{u}}))d\tau}, \quad \phi_j(s,\bar{\mathbf{u}}) = \mathbf{q}_j^\top \bar{\mathbf{u}}(s) + \mathbf{g}_j(\bar{\mathbf{u}})^\top \bar{\mathbf{u}}(s) + \mathbf{r}_j^\top \bar{\mathbf{f}}(s) \tag{30}$$

with suitable coefficients $\mathbf{p}_j, \mathbf{d}_j, \mathbf{q}_j, \mathbf{g}_j, \mathbf{r}_j \in \mathbb{R}^N$ and decay rates $\lambda_j, e_j(\bar{\mathbf{u}}) > 0$, that need to be identified from data.

Define the hidden states as,

$$\beta_j(t) = \int_0^t \mathcal{K}_j(s,\bar{\mathbf{u}})\phi_j(s,\bar{\mathbf{u}})ds \tag{31}$$

then through its differentiation with respect to time,

$$\dot{\beta}_j(t) = -\left[\lambda_j + e_j(\bar{\mathbf{u}})\right]\beta_j(t) + \mathbf{q}_j^\top \bar{\mathbf{u}}(t) + \mathbf{g}_j(\bar{\mathbf{u}})^\top \bar{\mathbf{u}}(t) + \mathbf{r}_j^\top \bar{\mathbf{f}}(t) \tag{32}$$

and the memory term becomes,

$$\int_0^t \boldsymbol{\kappa}(t,s,\bar{\mathbf{u}})ds = \sum_{j=1}^{m} \left[\mathbf{p}_j + \mathbf{d}_j(\bar{\mathbf{u}})\right]\beta_j(t) \tag{33}$$

Then, eq. (28b) is recast as the extended Markovian system,

$$\bar{\mathbf{A}}(\bar{\mathbf{u}})\dot{\bar{\mathbf{u}}} = \bar{\mathbf{B}}(\bar{\mathbf{u}})\bar{\mathbf{u}} + \left[\mathbf{P} + \mathbf{D}(\bar{\mathbf{u}})\right]\boldsymbol{\beta} + \bar{\mathbf{f}}(t) \tag{34a}$$

$$\dot{\boldsymbol{\beta}} = \left[\mathbf{Q} + \mathbf{G}(\bar{\mathbf{u}})\right]\bar{\mathbf{u}} + \left[\mathbf{E}(\bar{\mathbf{u}}) - \boldsymbol{\Lambda}\right]\boldsymbol{\beta} + \mathbf{R}\bar{\mathbf{f}}(t) \tag{34b}$$

where the data-driven operators associated to the hidden dynamics are collected as,

$$\boldsymbol{\Lambda} = \mathrm{diag}\left(\lambda_1, \lambda_2, \ldots, \lambda_m\right) \in \mathbb{R}^{m\times m}, \qquad \mathbf{P} = \left[\mathbf{p}_1, \mathbf{p}_2, \ldots, \mathbf{p}_m\right] \in \mathbb{R}^{N\times m} \tag{35a}$$

$$\mathbf{D}(\bar{\mathbf{u}}) = \left[\mathbf{d}_1(\bar{\mathbf{u}}), \mathbf{d}_2(\bar{\mathbf{u}}), \ldots, \mathbf{d}_m(\bar{\mathbf{u}})\right] \in \mathbb{R}^{N\times m}, \qquad \mathbf{Q} = \left[\mathbf{q}_1, \mathbf{q}_2, \ldots, \mathbf{q}_m\right] \in \mathbb{R}^{m\times N} \tag{35b}$$

$$\mathbf{G}(\bar{\mathbf{u}}) = \left[\mathbf{g}_1(\bar{\mathbf{u}}), \mathbf{g}_2(\bar{\mathbf{u}}), \ldots, \mathbf{g}_m(\bar{\mathbf{u}})\right] \in \mathbb{R}^{m\times N}, \qquad \mathbf{R} = \left[\mathbf{r}_1, \mathbf{r}_2, \ldots, \mathbf{r}_m\right] \in \mathbb{R}^{m\times N} \tag{35c}$$

$$\mathbf{E}(\bar{\mathbf{u}}) = \mathrm{diag}\left(e_1(\bar{\mathbf{u}}), e_2(\bar{\mathbf{u}}), \ldots, e_m(\bar{\mathbf{u}})\right) \in \mathbb{R}^{m\times m} \tag{35d}$$

The form of the temperature-dependent matrices $\mathbf{D}(\bar{\mathbf{u}})$, $\mathbf{G}(\bar{\mathbf{u}})$, and $\mathbf{E}(\bar{\mathbf{u}})$ is provided in the next section. Note that since the hidden states $\boldsymbol{\beta}$ serve as the memory, their initial conditions

are set to zero, i.e., $\boldsymbol{\beta}(t_0) = \mathbf{0}$, no memory at the beginning. The physics-infused model in eq. (34b) retains the structure of the LCM, while the hidden states account for missing physics through corrections to the stiffness and advection matrices, as well as the forcing term.

3.2.2 Coupled Physics-Infused Model

The next step involves coupling the physics-infused model in eq. (34b) with the SVM in eq. (13) to form the PIROM for ablating TPS. To this end, define the observables as the surface temperature $\mathbf{z}_u \in \mathbb{R}^{\tilde{N}}$ and displacements $\mathbf{z}_w \in \mathbb{R}^{\tilde{N}}$ for $\tilde{N} \leq N$ ablating surfaces to define the observable vector as $\mathbf{z} = [\mathbf{z}_u, \mathbf{z}_w]^\top \in \mathbb{R}^{n_z}$ with $n_z = 2\tilde{N}$ as the total number of observables.

Collect the RPM and hidden states into a single state vector $\mathbf{y} = [\bar{\mathbf{u}}, \mathbf{w}, \boldsymbol{\beta}]^\top \in \mathbb{R}^{n_y}$, where $n_y = N + \tilde{N} + m$, and define a data-driven operator $\mathbf{M} \in \mathbb{R}^{n_z \times n_y}$ to define the PIROM's observable as,

$$\mathbf{z} = \mathbf{M}\mathbf{y} \tag{36}$$

where,

$$\mathbf{M} = \begin{bmatrix} \mathbf{M}_{\bar{u}} & \mathbf{0} & \mathbf{M}_{\beta} \\ \mathbf{0} & \mathbf{I} & \mathbf{0} \end{bmatrix} \tag{37}$$

includes the matrices $\mathbf{M}_{\bar{u}} \in \mathbb{R}^{\tilde{N} \times N}$ and $\mathbf{M}_{\beta} \in \mathbb{R}^{\tilde{N} \times m}$, which computes the surface temperature observable from the RPM states and hidden states, respectively. Then, the PIROM is coupled to the SVM in eq. (13) by computing the surface recession velocity based on the PIROM's surface temperature prediction $\mathbf{z}_u$. Specifically, the surface recession velocity is updated as,

$$\dot{\mathbf{w}} = \boldsymbol{\Xi}\mathbf{z}_u - \tilde{\mathbf{f}} \tag{38}$$

Thus, the PIROM is formally stated as,

$$\boldsymbol{\mathcal{A}}\dot{\mathbf{y}} = [\boldsymbol{\mathcal{B}} + \boldsymbol{\mathcal{C}}]\,\mathbf{y} + \boldsymbol{\mathcal{F}}(t) \tag{39a}$$

$$\mathbf{z} = \mathbf{M}\mathbf{y} \tag{39b}$$

where,

$$\boldsymbol{\mathcal{A}} = \begin{bmatrix} \bar{\mathbf{A}} & \mathbf{O} & \mathbf{O} \\ \mathbf{O} & \mathbf{I} & \mathbf{O} \\ \mathbf{O} & \mathbf{O} & \mathbf{I} \end{bmatrix} \in \mathbb{R}^{n_y \times n_y}, \quad \boldsymbol{\mathcal{B}} = \begin{bmatrix} \bar{\mathbf{B}} & \mathbf{O} & \mathbf{P} \\ \boldsymbol{\Xi}\mathbf{M}_u & \mathbf{O} & \boldsymbol{\Xi}\mathbf{M}_\beta \\ \mathbf{Q} & \mathbf{O} & -\boldsymbol{\Lambda} \end{bmatrix} \in \mathbb{R}^{n_y \times n_y}, \tag{40a}$$

$$\boldsymbol{\mathcal{C}} = \begin{bmatrix} \mathbf{O} & \mathbf{O} & \mathbf{D}(\bar{\mathbf{u}}) \\ \mathbf{O} & \mathbf{O} & \mathbf{O} \\ \mathbf{G}(\bar{\mathbf{u}}) & \mathbf{O} & \mathbf{E}(\bar{\mathbf{u}}) \end{bmatrix} \in \mathbb{R}^{n_y \times n_y}, \quad \boldsymbol{\mathcal{F}} = \begin{bmatrix} \bar{\mathbf{f}}(t) \\ -\tilde{\mathbf{f}} \\ \mathbf{R}\bar{\mathbf{f}}(t) \end{bmatrix} \in \mathbb{R}^{n_y} \tag{40b}$$

The learnable parameters in the PIROM are collected as,

$$\boldsymbol{\Theta} = \{\mathbf{P}, \mathbf{Q}, \mathbf{R}, \mathbf{D}(\bar{\mathbf{u}}), \mathbf{G}(\bar{\mathbf{u}}), \mathbf{E}(\bar{\mathbf{u}}), \mathbf{M}_u, \mathbf{M}_\beta\}, \in \mathbb{R}^{n_\theta} \tag{41}$$

Particularly, the matrices $\mathbf{P}, \boldsymbol{\Lambda}, \mathbf{Q}, \mathbf{R}$ are constants that need to be identified from data, and account for the effects of coarse-graining on the stiffness and forcing matrices. The matrices $\mathbf{D}(\bar{\mathbf{u}}), \mathbf{E}(\bar{\mathbf{u}}), \mathbf{G}(\bar{\mathbf{u}})$ are state-dependent matrices, and account for the effects of coarse-graining on the advection matrix due to mesh motion. Leveraging the DG-FEM formula for the advection matrix in eq. (50c) in the Appendix, and noting that the ablating velocity in eq. (4) imposes the boundary condition for the mesh motion, the state-dependent matrices for the i-th component are written as,

$$\mathbf{D}(\bar{\mathbf{u}}) \approx \dot{\mathbf{w}}(\bar{\mathbf{u}}) \odot_{\mathrm{r}} \mathbf{D}, \quad \mathbf{G}(\bar{\mathbf{u}}) \approx \mathbf{G} \odot_{\mathrm{r}} \dot{\mathbf{w}}(\bar{\mathbf{u}}), \quad \mathbf{E}(\bar{\mathbf{u}}) \approx \dot{\mathbf{W}}(\bar{\mathbf{u}}) \odot \mathbf{E} \tag{42}$$

where $\dot{\mathbf{w}}(\bar{\mathbf{u}})$ is the SVM based on the observable temperature $\bar{\mathbf{u}}$, $\odot_{\mathrm{r}}$ is the row-wise multiplication, and $\dot{\mathbf{W}}$ is the concatenation of $\dot{\mathbf{w}}$ for $\tilde{m}$ times, where $\tilde{m}$ corresponds to the number of hidden states per component, i.e., $m = N\tilde{m}$.

The PIROM in eq. (39b) incorporates explicit information on the material properties, boundary conditions, and surface recession, and is designed to generalize across parametric variations in these inputs. Moreover, the hidden dynamics in eq. (34b) are interpretable, as these retain the functional form of the DG-FEM in eq. (8). The next step is focused on identifying the unknown data-driven parameters $\boldsymbol{\Theta}$ characterizing the hidden dynamics.

3.3 Learning the Hidden Dynamics

The learning of the PIROM is achieved through a neural-ODE like approach Chen2018. For ease of presentation, consider the following compact form of the PIROM in eq. (39b),

$$\boldsymbol{\mathcal{F}}\left(\dot{\mathbf{y}}, \mathbf{y}; \boldsymbol{\xi}, \boldsymbol{\Theta}\right) = \mathbf{0} \tag{43}$$

where $\boldsymbol{\xi}$ defines the parametrization of the problem, i.e., operating conditions, such as the BC's, as well as the material properties. Consider a dataset of N_s high-fidelity trajectories of observables over a time interval $[t_0, t_f]$,

$$\mathcal{D} = \left\{ \left(t_k, \mathbf{z}_{\mathrm{HF}}^{(l)}(t_k), \boldsymbol{\xi}^{(l)} \right) \right\}_{l=1}^{N_s}, \quad k = 0, 1, \ldots, K \tag{44}$$

The learning problem is formulated as the following differentially-constrained problem,

$$\min_{\boldsymbol{\Theta}} \quad \frac{1}{N_s} \sum_{l=1}^{N_s} \frac{1}{K} \sum_{k=0}^{K} \left\| \mathbf{z}_{\mathrm{HF}}^{(l)}(t_k) - \mathbf{M}\mathbf{y}^{(l)}(t_k) \right\|_2^2 \tag{45a}$$

$$\text{s.t.} \quad \boldsymbol{\mathcal{F}} \left(\dot{\mathbf{y}}^{(l)}, \mathbf{y}^{(l)}; \boldsymbol{\xi}^{(l)}, \boldsymbol{\Theta} \right) = \mathbf{0}, \quad t \in [t_0, t_f], \quad l = 1, 2, \ldots, N_s \tag{45b}$$

$$\mathbf{y}^{(l)}(t_0) = \mathbf{y}_0(\boldsymbol{\xi}^{(l)}), \quad l = 1, 2, \ldots, N_s \tag{45c}$$

4 Application to Thermal Protection Systems

In this section,

5 Conclusions

A Technical Details

This appendix presents the technical details of the PIROM framework applied to the TPS ablation problem. The first section provides the mathematical details for the definition of the DG-FEM. The second section follows the projection procedures from Ref. x , and demonstrates the effects of coarse-graining on the advection matrix. The third section presents the derivation of the LCM model from an energy-conservation perspective.

A.1 Full-Order Model

To obtain the full-order numerical solution, the governing equation is spatially discretized using variational principles of Discontinuous Galerkin (DG) to result in a high-dimensional system of ordinary differential equations (ODEs). The DG-FEM model is written in an element-wise form, which is beneficial for subsequent derivations of the lower-order models. Note that the choice of DG approach here is mainly for theoretical convenience in the subsequent coarse-graining formulation. In the numerical results, the full-order TPS ablation simulations is computed using standard FEM instead, and the equivalence between DG and standard FEM is noted upon their convergence.

A.1.1 Domain Discretization

Consider a conforming mesh partition of the domain, as shown in Fig. DOMAIN , where each element belongs to one and only one component. Denote the collection of all M elements as $\{E_i\}_{i=1}^{M}$. To ease the description of the DG model, a graph structure is employed. The elements are treated as vertices, the set of which is denoted $\mathcal{V} = \{m\}_{m=1}^{M}$. Two neighboring elements, E_i and E_j, are connected by an edge (i, j), and the shared boundary between them is denoted e_{ij}. The collection of all edges are denoted $\mathcal{E}$, and $\mathcal{G}$ is referred to as a graph. In the graph, the edges are unidirected, meaning if $(i, j) \in \mathcal{E}$ then $(j, i) \in \mathcal{E}$. Furthermore, denote the neighbors of the i-th element as $\mathcal{N}_i = \{j|(i, j) \in \mathcal{E}\}$. Lastly, for the ease of notation, introduce two special indices: T for the boundary of an element that overlaps with the Dirichlet boundary condition, and similarly q for the Neumann boundary condition.

A.1.2 Weak Form of Discontinuous Galerkin Method

Choosing appropriate basis functions ϕ_k and ϕ_l and using the Interior Penalty Galerkin (IPG) scheme [3], the variational bilinear form for eq. (1a) is,

$$\sum_{i=1}^{M} a_{\epsilon,i}(\phi_k, \phi_l) = \sum_{i=1}^{M} L_i(\phi_k) \tag{46}$$

where ϵ is an user-specified parameter and,

$$a_{\epsilon,i}(\phi_k, \phi_l) = \int_{E^{(i)}} \left(\rho c_p \phi_k \frac{\partial \phi_l}{\partial t} + \nabla \phi_k \cdot (\mathbf{k} \nabla \phi_l) - \rho c_p \phi_k \mathbf{v} \cdot \nabla \phi_l \right) dE^{(i)} \tag{47a}$$

$$= - \sum_{j \in \mathcal{N}_i \cup \{T_b\}} \int_{e_{ij}} \{\mathbf{k} \nabla \phi_k \cdot n\} [\phi_l] \, de_{ij} + \epsilon \sum_{j \in \mathcal{N}_i \cup \{T_b\}} \int_{e_{ij}} \{\mathbf{k} \nabla \phi_l \cdot n\} [\phi_k] \, de_{ij}$$

$$+ \sigma \sum_{j \in \mathcal{N}_i \cup \{T_b\}} \int_{e_{ij}} [\phi_k] [\phi_l] \, de_{ij} \tag{47b}$$

$$L_i(v) = \epsilon \sum_{j \in \mathcal{N}_i \cup \{T_b\}} \int_{e_{ij}} (\mathbf{k} \nabla \phi_l \cdot n) \, T_b de_{ij} + \int_{e_{iq}} \phi_k q_b de_{iq} + \sigma \int_{e_{iT}} \phi_k T_b de_{iT} \tag{47c}$$

In the bi-linear form above, the notations [] and {} are respectively the jumps and averages at the boundary e_{ij} share by two elements E_i and E_j,

$$[u] = u\big|_{E_i} - u\big|_{E_j}, \quad \{u\} = \frac{1}{2}\left(u\big|_{E_i} + u\big|_{E_j} \right), \quad \text{for } x \in e_{ij} = E_i \cap E_j$$

Furthermore, in the bi-linear form, the terms associated with σ are introduced to enforce the Dirichlet boundary conditions; σ is a penalty factor whose value can depend on the size of an element. Depending on the choice of ϵ, the bi-linear form corresponds to symmetric IPG ($\epsilon = -1$), non-symmetric IPG ($\epsilon = 1$), and incomplete IPG ($\epsilon = 0$). All these schemes are consistent with the original PDE and have similar convergence rate with respect to mesh size. In the following derivations, the case $\epsilon = 0$ is chosen for the sake of simplicity.

A.1.3 Discontinuous Galerkin Model

Next, the DG-based model is written in an element-wise form. For the i-th element, use a set of P trial functions to represent the temperature as in eq. (6). Without loss of generality, the trial functions are assumed to be orthogonal, so that $\int_{E^{(i)}} \phi_k^{(i)}(x) \phi_l^{(i)}(x) dx = \left|E^{(i)}\right| \delta_{kl}$, where $\left|E^{(i)}\right|$ is the area ($n_d = 2$) or volume ($n_d = 3$) of the i-th element, and δ_{kl} is the Kronecker delta.

Using test functions same as trial functions, the dynamics $\mathbf{u}^{(i)}$ is obtained by evaluating

the element-wise bi-linear forms,

$$a_{\epsilon,i}(\phi_k^{(i)}, T^{(i)}) = L_i(\phi_k^{(i)}), \quad k = 1, 2, \ldots, P \tag{48}$$

The above procedure yields,

$$\mathbf{A}^{(i)}\dot{\mathbf{u}}^{(i)} = \left(\mathbf{B}^{(i)} + \mathbf{C}^{(i)}(t)\right)\mathbf{u}^{(i)} + \sum_{j \in \mathcal{N}_i \cup \{T_b\}} \left(\mathbf{B}_{ij}^{(i)}\mathbf{u}^{(i)} + \mathbf{B}_{ij}^{(j)}\mathbf{u}^{(j)}\right) + \mathbf{f}^{(i)}(t) \tag{49}$$

where for $k, l = 1, 2, \ldots, P$,

$$\left[\mathbf{A}^{(i)}\right]_{kl} = \int_{E^{(i)}} \rho c_p \phi_k^{(i)} \phi_l^{(i)} dE^{(i)} \tag{50a}$$

$$\left[\mathbf{B}^{(i)}\right]_{kl} = -\int_{E^{(i)}} \left(\nabla \phi_k^{(i)}\right) \cdot \left(\mathbf{k} \nabla \phi_l^{(i)}\right) dE^{(i)} \tag{50b}$$

$$\left[\mathbf{C}^{(i)}\right]_{kl} = \int_{E^{(i)}} \rho c_p \phi_k^{(i)} \mathbf{v}^{(i)} \cdot \nabla \phi_l^{(i)} dE^{(i)} \tag{50c}$$

$$\left[\mathbf{B}_{ij}^{(i)}\right] = \int_{e_{ij}} \left\{\mathbf{k} \nabla \phi_k^{(i)} \cdot \hat{n}\right\} \phi_l^{(i)} - \sigma \left[\phi_k^{(i)}\right] \phi_l^{(i)} de_{ij} \tag{50d}$$

$$\left[\mathbf{B}_{ij}^{(j)}\right] = \int_{e_{ij}} -\left\{\mathbf{k} \nabla \phi_k^{(i)} \cdot \hat{n}\right\} \phi_l^{(j)} + \sigma \left[\phi_k^{(i)}\right] \phi_l^{(j)} de_{ij} \tag{50e}$$

$$\left[\mathbf{f}^{(i)}\right]_k = \int_{e_{iq}} \phi_k^{(i)} q_b de_{iq} + \sigma \int_{e_{iT}} \phi_k^{(i)} de_{iT} \tag{50f}$$

The matrices $\mathbf{A}^{(i)} \in \mathbb{R}^{P \times P}$, $\mathbf{B}^{(i)} \in \mathbb{R}^{P \times P}$, and $\mathbf{C}^{(i)} \in \mathbb{R}^{P \times P}$ are respectively the capacitance, conductivity, and advection matrices for element i. These matrices depend on ρ, c_p, $\mathbf{k}$, and $\mathbf{v}$, and hence can be non-linear functions of $\mathbf{u}^{(i)}$. Since the trial functions are orthogonal, if ρc_p is constant within an element, $\mathbf{A}^{(i)}$ is diagonal; otherwise, $\mathbf{A}_i$ is symmetric and positive definite as $\rho c_p > 0$.

For compactness, the element-wise model in eq. (49) is also written in matrix form,

$$\mathbf{A}(\dot{\mathbf{u}}) = [\mathbf{B}(\mathbf{u}) + \mathbf{C}(\mathbf{u})]\,\mathbf{u} + \mathbf{f}(t) \tag{51}$$

where $\mathbf{u} = \left[\mathbf{u}^{(1)}, \mathbf{u}^{(2)}, \cdots, \mathbf{u}^{(M)}\right]^T \in \mathbb{R}^{MP}$ includes all DG variables, $\mathbf{f} = \left[\mathbf{f}^{(1)}, \mathbf{f}^{(2)}, \ldots, \mathbf{f}^{(M)}\right]^T \in \mathbb{R}^{MP}$, $\mathbf{A}$ and $\mathbf{C}$ are matrices of M diagonal blocks whose i-th blocks are $\mathbf{A}^{(i)}$ and $\mathbf{C}^{(i)}$, and $\mathbf{B}$ is a matrix of $M \times M$ blocks whose (i, j)-th block is,

$$\mathbf{B}_{ij} = \begin{cases} \mathbf{B}^{(i)} + \sum_{j \in \mathcal{N}_i \cup \{T_b\}} \mathbf{B}_{ij}^{(i)}, & i = j \\ \mathbf{B}_{ij}^{(j)}, & i \neq j \end{cases} \tag{52}$$

The dependency of $\mathbf{A}$, $\mathbf{B}$, and $\mathbf{C}$ on $\mathbf{u}$ is explicitly noted in eq. (51), which is the source of non-linearity in the current TPS problem. Moreover, the mesh velocity $\mathbf{v}$ varies with space and time, and thus the advection matrix $\mathbf{C}$ varies with time as a function of q_b.

A.2 Coarse-Graining of Dynamics

The LCM is obtained by coarse-graining the full-order DG-FEM. This coarse-graining procedure produces resolved $\mathbf{r}^{(1)}(\mathbf{u},t)$ and residual $\mathbf{r}^{(2)}(\mathbf{u},t)$ dynamics as in eq. (23). This section presents the detail derivations and magnitude analysis for the resolved and residual dynamics.

A.2.1 Resolved Dynamics

Using eq. (20), the resolved dynamics is computed as follows,

$$\mathbf{r}^{(1)}(\mathbf{u},t) = \mathcal{P}\left[\mathbf{\Phi}^{+}\mathbf{A}(\mathbf{u})^{-1}\left(\mathbf{B}(\mathbf{u})\mathbf{u}+\mathbf{C}(\mathbf{u})\mathbf{u}+\mathbf{f}(t)\right)\right] \tag{53a}$$

$$\begin{aligned}=\mathbf{\Phi}^{+}\mathbf{A}\left(\mathbf{P}\mathbf{u}\right)^{-1}\mathbf{P}\mathbf{B}\left(\mathbf{P}\mathbf{u}\right)\mathbf{P}\mathbf{u} &+\mathbf{\Phi}^{+}\mathbf{A}\left(\mathbf{P}\mathbf{u}\right)^{-1}\mathbf{P}\mathbf{C}\left(\mathbf{P}\mathbf{u}\right)\mathbf{P}\mathbf{u}\\ &+\mathbf{\Phi}^{+}\mathbf{A}\left(\mathbf{P}\mathbf{u}\right)^{-1}\mathbf{P}\mathbf{f}(t,\mathbf{P}\mathbf{u})\end{aligned} \tag{53b}$$

$$\begin{aligned}=\underbrace{\mathbf{\Phi}^{+}\mathbf{A}\left(\mathbf{\Phi}\bar{\mathbf{u}}\right)^{-1}\mathbf{\Phi}}_{\#1}\underbrace{\mathbf{\Phi}^{+}\mathbf{B}\left(\mathbf{\Phi}\bar{\mathbf{u}}\right)\mathbf{\Phi}\bar{\mathbf{u}}}_{\#2} &+\mathbf{\Phi}^{+}\mathbf{A}\left(\mathbf{\Phi}\bar{\mathbf{u}}\right)^{-1}\mathbf{\Phi}\underbrace{\mathbf{\Phi}^{+}\mathbf{C}\left(\mathbf{\Phi}\bar{\mathbf{u}}\right)\mathbf{\Phi}}_{\#3}\bar{\mathbf{u}}\\ &+\mathbf{\Phi}^{+}\mathbf{A}\left(\mathbf{\Phi}\bar{\mathbf{u}}\right)^{-1}\mathbf{\Phi}\underbrace{\mathbf{\Phi}^{+}\mathbf{f}(t,\mathbf{\Phi}\bar{\mathbf{u}})}_{\#4}\end{aligned} \tag{53c}$$

Detailed derivations for the #1, #2, and #4 terms can be found in Ref. x. The effects of coarse-graining on the advection term #3 are analyzed next.

Term #3 The $\mathbf{C}(\mathbf{u}) \in \mathbb{R}^{MP\times MP}$ matrix contains M diagonal of size $P\times P$, since the basis functions are defined locally on each element. Therefore, $\left[\mathbf{C}(\mathbf{u})\right]_{ij} = \mathbf{0}$ for all $i \neq j$ with $i,j = 1,2,\ldots,M$. It follows that for $k,l = 1,2,\cdots,N$,

$$\left[\mathbf{\Phi}^{+}\mathbf{C}(t,\mathbf{\Phi}\bar{\mathbf{u}})\mathbf{\Phi}\right]_{kl} = \sum_{i=1}^{M}\sum_{j=1}^{M}\boldsymbol{\varphi}_i^{k+}\left[\mathbf{C}(t,\mathbf{\Phi}\bar{\mathbf{u}})\right]_{ij}\boldsymbol{\varphi}_j^{l} \tag{54a}$$

$$= \sum_{i=1}^{M}\boldsymbol{\varphi}_i^{k+}\left[\mathbf{C}(t,\mathbf{\Phi}\bar{\mathbf{u}})\right]_{ii}\boldsymbol{\varphi}_i^{l} \tag{54b}$$

$$= \sum_{i\in\mathcal{V}_k}\boldsymbol{\varphi}_i^{k+}\left[\mathbf{C}(t,\mathbf{\Phi}\bar{\mathbf{u}})\right]_{ii}\boldsymbol{\varphi}_i^{l} \tag{54c}$$

where in the second row, the fact that $[\mathbf{C}(\mathbf{u})]_{ij} = 0$ for all $i \neq j$ is used, and in the last row, the fact that $\boldsymbol{\varphi}_i^{k+} = 0$ for all $i \notin \mathcal{V}_k$ is used. Now, considering that $[\mathbf{C}(\mathbf{u})]_{ii}$ has a $(1,1)$-th zero element, i.e., $[C_{11}(t, \boldsymbol{\Phi}\bar{\mathbf{u}})]_{ii} = 0$, and that if $k \neq l$ then $i \notin \mathcal{V}_l$ and thus $\boldsymbol{\varphi}_i^l = \mathbf{0}$, it follows that for some index $i \in \mathcal{V}_k$,

$$\boldsymbol{\varphi}_i^{k+} \left[\mathbf{C}(t, \boldsymbol{\Phi}\bar{\mathbf{u}})\right]_{ii} \boldsymbol{\varphi}_i^l = \boldsymbol{\varphi}_i^{k+} \left[\mathbf{C}(t, \boldsymbol{\Phi}\bar{\mathbf{u}})\right]_{ii} \boldsymbol{\varphi}_i^k = \frac{|E_i|}{|\Omega_k|} \left[C_{11}(t, \boldsymbol{\Phi}\bar{\mathbf{u}})\right]_{ii} = 0 \tag{55}$$

The matrix $\left[\boldsymbol{\Phi}^+ \mathbf{C}(t, \boldsymbol{\Phi}\bar{\mathbf{u}})\boldsymbol{\Phi}\right]_{kl} = 0$ for all $k, l = 1, 2, \ldots, N$, and thus,

$$\bar{\mathbf{C}}\left(t, \bar{\mathbf{u}}\right) = \boldsymbol{\Phi}^+ \mathbf{C}\left(t, \boldsymbol{\Phi}\bar{\mathbf{u}}\right) \boldsymbol{\Phi} = \mathbf{0} \tag{56}$$

as indicated by the LCM in eq. (9).

A.2.2 Magnitude Analysis for Residual Dynamics

Next, the magnitude of the residual dynamics $\mathbf{r}^{(2)}(\mathbf{u}, t)$ is analyzed to pinpoint the missing physics in the LCM. By definition,

$$\begin{aligned}
\mathbf{r}^{(2)}(\mathbf{u}, t) &= \dot{\bar{\mathbf{u}}} - \mathbf{r}^{(1)}(\bar{\mathbf{u}}, t) && \text{(57a)}\\
&= \boldsymbol{\Phi}^+ \mathbf{r}(\mathbf{u}, t) - \mathbf{r}^{(1)}(\mathbf{u}, t) && \text{(57b)}\\
&= \underbrace{\boldsymbol{\Phi}^+ \mathbf{A}(\mathbf{u})^{-1} \mathbf{B}(\mathbf{u})\mathbf{u} - \bar{\mathbf{A}}(\bar{\mathbf{u}})^{-1} \bar{\mathbf{B}}(\bar{\mathbf{u}})\bar{\mathbf{u}}}_{\#1} + \underbrace{\boldsymbol{\Phi}^+ \mathbf{A}(\mathbf{u})^{-1} \mathbf{C}(\mathbf{u})\mathbf{u} - \bar{\mathbf{A}}(\bar{\mathbf{u}})^{-1} \bar{\mathbf{C}}(t, \bar{\mathbf{u}})\bar{\mathbf{u}}}_{\#2}\\
&\qquad + \underbrace{\boldsymbol{\Phi}^+ \mathbf{A}(\mathbf{u})^{-1} \mathbf{f}(t) - \bar{\mathbf{A}}(\bar{\mathbf{u}})^{-1} \bar{\mathbf{f}}(t)}_{\#3} && \text{(57c)}
\end{aligned}$$

The magnitude analysis for terms #1 and #3 can be found in Ref. x. The analysis for term #2 is presented next. Let $\mathbf{D}(\bar{\mathbf{u}}) = \mathbf{A}(\boldsymbol{\Phi}\bar{\mathbf{u}})^{-1} \mathbf{P}\mathbf{C}(t, \boldsymbol{\Phi}\bar{\mathbf{u}})$, then,

$$\begin{aligned}
&\boldsymbol{\Phi}^+ \mathbf{A}(\mathbf{u})^{-1} \mathbf{C}(\mathbf{u})\mathbf{u} - \bar{\mathbf{A}}(\bar{\mathbf{u}})^{-1} \bar{\mathbf{C}}(t, \bar{\mathbf{u}})\bar{\mathbf{u}} && \text{(58a)}\\
&= \boldsymbol{\Phi}^+ \mathbf{A}(\mathbf{u})^{-1} \mathbf{C}(\mathbf{u})\mathbf{u} - \boldsymbol{\Phi}^+ \mathbf{A}(\boldsymbol{\Phi}\bar{\mathbf{u}})^{-1} \mathbf{P}\mathbf{C}(t, \boldsymbol{\Phi}\bar{\mathbf{u}})\boldsymbol{\Phi}\boldsymbol{\Phi}^+ \mathbf{u} && \text{(58b)}\\
&= \boldsymbol{\Phi}^+ \mathbf{A}^{-1}(\mathbf{u}) \mathbf{C}(\mathbf{u})\mathbf{u} - \boldsymbol{\Phi}^+ \mathbf{D}(\bar{\mathbf{u}})\boldsymbol{\Phi}\boldsymbol{\Phi}^+ \mathbf{u} && \text{(58c)}\\
& && \text{(58d)}
\end{aligned}$$

where $\mathbf{P} = \mathbf{\Phi}\mathbf{\Phi}^+$. Thus,

$$\left\|\mathbf{\Phi}^+\mathbf{A}(\mathbf{u})^{-1}\mathbf{C}(\mathbf{u})\mathbf{u} - \bar{\mathbf{A}}^{-1}(\bar{\mathbf{u}})\bar{\mathbf{C}}(t,\bar{\mathbf{u}})\bar{\mathbf{u}}\right\| \tag{59a}$$

$$\leq \left\|\mathbf{\Phi}^+\mathbf{A}^{-1}(\mathbf{u})\mathbf{C}(\mathbf{u})\mathbf{u} - \mathbf{\Phi}^+\mathbf{D}(\bar{\mathbf{u}})\mathbf{u}\right\| + \left\|\mathbf{\Phi}^+\mathbf{D}(\bar{\mathbf{u}})\mathbf{u} - \mathbf{\Phi}^+\mathbf{D}(\bar{\mathbf{u}})\mathbf{\Phi}\mathbf{\Phi}^+\mathbf{u}\right\| \tag{59b}$$

$$\leq \left\|\mathbf{\Phi}^+\right\| \underbrace{\left\|\mathbf{A}^{-1}(\mathbf{u})\mathbf{C}(\mathbf{u})\mathbf{u} - \mathbf{D}(\bar{\mathbf{u}})\mathbf{u}\right\|}_{\#1} + \left\|\mathbf{\Phi}^+\mathbf{D}(\bar{\mathbf{u}})\right\| \underbrace{\left\|\mathbf{u} - \mathbf{\Phi}\mathbf{\Phi}^+\mathbf{u}\right\|}_{\#2} \tag{59c}$$

where term #2 is due to the apprixiamation of non-uniform temperaeture as constants, and term #1 is the error in the advection dynamics due to coarse-graining.

A.3 Lumped Capacitance Model

The following assumptions are employed: (1) the temperature in component (i) is described by a scalar time-varying average temperature $\bar{u}^{(i)}$, (2) between neighboring components (i) and (j) the heat flux is approximated as,

$$q_{ij} = \frac{\bar{u}^{(j)} - \bar{u}^{(i)}}{R_{ij}} \tag{60}$$

where R_{ij} is the thermal resistance. Empirically, for a component of isotropic heat conductivity k, length ℓ, and cross-section area A, the thermal resistance is $R = \ell/kA$. Between components i and j, define $R_{ij} = R_i + R_j$. In addition, the heat flux due to Dirichlet boundary condition is computed as $q_{iT} = (T_b - \bar{u}^{(i)})/R_i$.

At component i, the dynamics of LCM are given by,

$$\int_{E^{(i)}} \rho c_p \dot{\bar{u}}^{(i)} dE^{(i)} = \left(\sum_{j\in\mathcal{N}_i} \int_{e_{ij}} \frac{\bar{u}^{(j)} - \bar{u}^{(i)}}{R_{ij}} de_{ij}\right) + \int_{e_{iq}} q_b de_{iq} + \int_{e_{iT}} \frac{T_b - \bar{u}^{(i)}}{R_i} de_{iT} \tag{61a}$$

$$\bar{A}^{(i)}\dot{\bar{u}}^{(i)} = \left(\sum_{j\in\mathcal{N}_i} \frac{|e_{ij}|}{R_{ij}}\left(\bar{u}^{(j)} - \bar{u}^{(i)}\right)\right) + |e_{iq}|\bar{q}^{(i)} + \frac{|e_{iT}|}{R_i}\left(\bar{T}^{(i)} - \bar{u}^{(i)}\right) \tag{61b}$$

$$= \sum_{j\in\mathcal{N}_i}\left(-\frac{|e_{ij}|}{R_{ij}}\bar{u}^{(i)} + \frac{|e_{ij}|}{R_{ij}}\bar{u}^{(j)}\right) + \left(-\frac{|e_{iT}|}{R_i}\bar{u}^{(i)}\right) + \left(|e_{iq}|\bar{q}^{(i)} + \frac{|e_{iT}|}{R_i}\bar{T}^{(i)}\right) \tag{61c}$$

$$= \sum_{j\in\mathcal{N}_i\cup\{T_b\}}\left(\bar{B}_{ij}^{(i)}\bar{u}^{(i)} + \bar{B}_{ij}^{(j)}\bar{u}^{(j)}\right) + \bar{f}^{(i)} \tag{61d}$$

where in eq. (61b) $|e|$ denotes the length ($d = 2$) or area ($d = 3$) of a component boundary e. The $\bar{A}^{(i)}$, $\bar{B}_{ij}^{(i)}$, and $\bar{B}_{ij}^{(j)}$ quantities are provided in eq. (12).

The lumped-mass representation for the four-component TPS is shown in Fig. 2. Let v_i

represent the area of the i-th element, $\overline{\rho c_p}_{,i}$, the heat capacity evaluated using the average temperature $\bar{u}^{(i)}$, and $1/R_{ij} = 1/R_i(\bar{u}^{(i)}) + 1/R_j(\bar{u}^{(j)})$ the equivalent thermal resistance between elements i and j. Leveraging the formulas from eqs. (11b) and (12), the LCM matrices are given by,

$$\bar{\mathbf{A}} = \begin{bmatrix} \overline{\rho c_p}_{,1} v_1 & 0 & 0 & 0 \\ 0 & \overline{\rho c_p}_{,2} v_2 & 0 & 0 \\ 0 & 0 & \overline{\rho c_p}_{,3} v_3 & 0 \\ 0 & 0 & 0 & \overline{\rho c_p}_{,4} v_4 \end{bmatrix}, \tag{62a}$$

$$\bar{\mathbf{B}} = \begin{bmatrix} \frac{1}{R_{12}} + \frac{1}{R_{14}} & -\frac{1}{R_{12}} & 0 & -\frac{1}{R_{14}} \\ -\frac{1}{R_{12}} & \frac{1}{R_{12}} + \frac{1}{R_{24}} + \frac{1}{R_{23}} & -\frac{1}{R_{23}} & -\frac{1}{R_{24}} \\ 0 & -\frac{1}{R_{32}} & \frac{1}{R_{32}} + \frac{1}{R_{34}} & -\frac{1}{R_{34}} \\ -\frac{1}{R_{14}} & -\frac{1}{R_{24}} & -\frac{1}{R_{34}} & \frac{1}{R_{14}} + \frac{1}{R_{24}} + \frac{1}{R_{34}} \end{bmatrix}, \quad \bar{\mathbf{f}} = \begin{bmatrix} \bar{q}^{(1)} \\ \bar{q}^{(2)} \\ \bar{q}^{(3)} \\ 0 \end{bmatrix} \tag{62b}$$

References

[1] Adam J. Amar, A. Brandon Oliver, Benjamin S. Kirk, Giovanni Salazar, and Justin Droba. Overview of the charring ablator response (char) code. In AIAA, editor, *AIAA Aviation Forum*, 2016.

[2] Guy L. Bergel, Frank B. Beckwith, Gabiel J. de Frias, Kevin M. Manktelow, Mark T. Merewether, Scott T. Miller, Krishen J. Parmar, Timothy S. Shelton, Jesse T. Thomas, Jeremy T. Trageser, Benjamin T. Treweek, Michael V. Veilleux, and Ellen B. Wagman. *Sierra/SolidMechanics 5.6 User's Manual*, 2022.

[3] Gary Cohen and Sebastien Pernet. *Finite Element and Discontinuous Galerkin Methods for Transient Wave Equations*. Springer Dordrecht, Le Chesnay and Toulouse France, 2018.

[4] Frank P. Incropera, David P. DeWitt, Theodore L. Bergman, and Adrienne S. Lavine. *Fundamentals of Heat and Mass Transfer*. Wiley, Hoboken, NJ, 7th edition, 2011.

[5] Eric Parish and Karthik Duraisamy. Non-markovian closure models for large eddy simulations using the mori-zwanzig formalism. *Phys. Rev. Fluids*, 2:014604, Jan 2017.

[6] Eric Parish and Karthik Duraisamy. A unified framework for multiscale modeling using the mori-zwanzig formalism and the variational multiscale method. *ArXiv*, 12 2017.

[7] Eric Parish and Karthik Duraisamy. *Coarse-Graining Turbulence Using the Mori–Zwanzig Formalism*. Cambridge University Press, Cambridge, 2025.

[8] Carlos A. Vargas Venegas, Daning Huang, Patrick Blonigan, and John Tencer. Physics-infused reduced-order modeling for analysis of multi-layered hypersonic thermal protection systems. *ArXiv*, 2025.

[9] Yin Yu, John Harlim, Daning Huang, and Yan Li. Learning coarse-grained dynamics on graph. *arXiv preprint arXiv:2405.09324*, 2024.